Research Article

Nanocrystals Growth Control during Laser Annealing of Sn:(α-Si) Composites

V. Neimash,[1] P. Shepelyavyi,[2] G. Dovbeshko,[1] A. O. Goushcha,[1] M. Isaiev,[3] V. Melnyk,[1] O. Didukh,[3] and A. Kuzmich[3]

[1]*Institute of Physics, National Academy of Sciences of Ukraine, 46 Prospekt Nauky, Kyiv 03028, Ukraine*
[2]*Institute of Semiconductor Physics, National Academy of Sciences of Ukraine, 45 Prospekt Nauky, Kyiv 03028, Ukraine*
[3]*Faculty of Physics, Taras Shevchenko National University of Kyiv, 64/13 Volodymyrska Street, Kyiv 01601, Ukraine*

Correspondence should be addressed to A. O. Goushcha; goushcha@cox.net

An efficient technique for low temperature metal-induced nanocrystalline silicon fabrication is presented. The technique is based on laser annealing of thin films of "amorphous silicon-tin" composites combined with in situ control and monitoring with Raman technique. Laser annealing was shown to provide the possibility of fine-tuning the nanocrystals size and concentration, which is important in photovoltaic and thermoelectric devices fabrication.

1. Introduction

Thin composite films "Si nanocrystals in an amorphous Si matrix" are considered as a promising material for the next-generation solar cells (SC) utilizing quantum dots [1]. This is because the composites possess a unique set of physical properties: direct band-gap mechanism of light absorption, band-gap dependence on the nanocrystals size, suppressed Staebler-Wronski effect, and suitability for fabrication using flexible substrates.

Using of silicon nanocomposites allows fundamentally increasing SC efficiency by creating polymorphic cascade type heterostructures [2, 3] and to reduce SC production cost through advantages of thin films roll-to-roll manufacturing technologies [4, 5]. Among the main problems that hinder practical implementation of the advantages of Si nanocrystals (nc-Si) is inadequate control of the size and concentration of Si nanocrystals at economically justified rates of films formation. Therefore, despite a large number of existing technologies of nc-Si production, much attention is still paid to their improvement and finding new alternatives. Among those are the advanced methods for micro- and nanocrystalline Si films growth using electron-cyclotron resonance chemical vapor deposition (CVD) [6], high deposition pressure at RF plasma

excitation frequencies [7], variations of the hot-wire CVD [8–10], optimization of plasma composition for CVD [11], and extended theoretical studies to improve crystallization processes (see, e.g., [12]).

Metal-induced crystallization (MIC) of amorphous silicon (α-Si) [13–17] is one of the most promising ways in this field. In particular, tin (Sn) stimulated formation of Si nanocrystals with sizes of 2–5 nm within the amorphous Si matrix at temperatures below 450°C was recently demonstrated [18–20]. The partial volume of the nanocrystalline phase of up to 80% was formed and experimental results were interpreted using new MIC mechanism proposed in the referenced works [20, 21], which was markedly different from the known mechanisms suggested for other metals [13, 15–17]. According to this mechanism, silicon nanocrystals are formed during cyclic processes of formation and disintegration of a supersaturated solution of silicon in Sn. The crystallization occurs in a narrow eutectic layer at the α-Si/Sn interface. In the current paper, we show that the process of Sn-induced crystallization can be initiated and sustained by laser light at relatively low power. We demonstrate that the Raman technique allows monitoring the sample temperature and simultaneously controlling the nanocrystals' size and partial
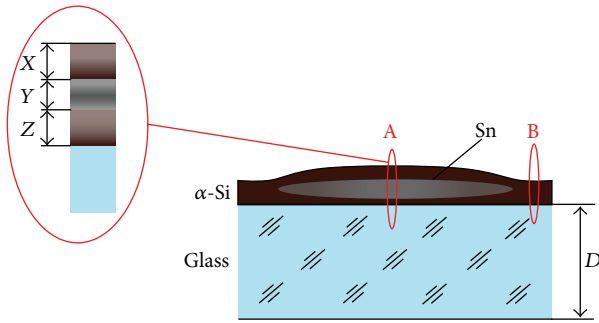
FIGURE 1: Cross-sectional schematics of the layered structures Si-Sn-Si. "A" and "B" are the two regions of the samples selectively studied in this work.

volume of the nanocrystalline phase by changing the intensity and duration of the laser radiation.

2. Materials and Methods

The samples for studies were made by spot ($76 \times 76 \, \text{mm}^2$) deposition of the electronics-grade silicon and tin (99.92%) using thermal evaporation in vacuum on the borosilicate glass wafer substrate (Figure 1). The temperature of the substrate was kept around 150°C during the deposition. The sandwich-type structures were formed by a sequential deposition of (i) α-Si layer with the thickness Z, (ii) tin layer with the thickness Y, and (iii) α-Si layer with the thickness X.

The layers thickness (X, Y, Z) was varied within the range from 50 to 200 nm with the step of 50 nm. All layers were deposited in the same vacuum chamber (10^{-3} Pa) using three different evaporators. The region of the sample that contained Sn layer sandwiched between two α-Si layers was shaped as a disk of diameter of 50 mm, located in the center of the square (76 mm × 76 mm) glass substrate. The regions of the sample between the edge of this disk and edges of the substrate did not contain Sn layer. The SEM images of the deposited samples within region A indicated in Figure 1 are shown in Figure 2.

The spherical features having diameter ranging from 200 to 500 nm in Figure 2 are typical for Si-Sn alloys [20] and heterostructures [21] obtained using thermal deposition in vacuum. It was shown in the recent works that these features contain metallic (Sn) cores (droplets) and shells of amorphous or combined amorphous/crystalline Si. Such spherical features were shown to form during the deposition of the second (top) layer of amorphous Si. The liquid metal (Sn) droplets are formed during the metal deposition at the substrate temperature higher than the Sn melting temperature of ~229°C. Thermal treatment of such structures at the temperatures higher than the Sn melting temperature initiates α-Si transformation within the shells into a nanocrystalline state. The mechanism of such transformation was discussed in the previous works [21, 22]. Due to the surface morphology of the sample shown in Figure 2, the light reflection from the surface of the sample is negligible. Visually, the surface appears like black soot, featuring thereby significant property of energy

loss minimization due to reflection, which is important for the solar cells industry.

As is known, rather efficient thermal crystallization of pure amorphous Si occurs at temperatures close to or above 1000°C [23]. For hydrogenated α-Si, the crystalline phase growth is significantly enhanced and occurs at a reasonably high rate at temperatures of ~500°C or higher [24, 25]. In contrast, MIC, in particular Sn-induced crystallization of pure α-Si, proceeds at significantly lower temperatures [14, 15, 21, 22], opening new opportunities for the structures as shown in Figures 1 and 2 through manufacturing of thin films of nanocrystalline Si on flexible and cheap polymer substrates.

The laser annealing is one of possible methods of initialization MIC thin films of amorphous silicon. This method allows also measuring Raman spectra in situ during the heating process. The analysis of Raman spectra makes it possible to monitor the temperature of annealing, the size of the formed nanocrystals, and their partial volume [26–30].

Both the laser annealing of prepared samples and measurements of Raman spectra were performed using the micro-Raman spectrometer Renishaw. As the light source, the laser radiation with the wavelength 633 nm and maximum power P_0 = 10 mW was used. The laser spot radius was either 1 μm or 2 μm; therefore, the maximum light intensity was I_0 = 3×10^5 W cm^{-2}. Raman spectra were recorded at room temperature in the two regions of the sample (see Figure 1): region A (containing Sn layer deposited between two α-Si layers) and region B (without Sn layer). Data collection in each experimental run continued for 30 s and three different irradiation intensities were used (I_1 = 0.1I_0; I_2 = 0.5I_0; I_3 = I_0). The forth experimental run was repeated at irradiation intensity I_4 = 0.1I_0. More Raman runs/scans were applied in some cases as necessary.

Raman spectra of the samples were recorded from the same area of the sample surface and under the same laser intensity several times. This allowed studying the accumulation dynamics of the nanocrystalline phase with irradiation time and, therefore, estimating the efficiency of laser-induced crystallization.

3. Results and Discussion

Raman spectra recorded from both regions A and B of all samples during the first run with the initial light intensity I_1 exhibited only a wide spectral band with the maximum near 475 cm^{-1}, corresponding to amorphous silicon. During the following experimental runs, the increase of irradiation intensity to I_2 and further to I_3 did not affect the spectra in the B region but resulted in a narrow peak appearance and rise around 490–520 cm^{-1} spectral range in the data, collected from region A (Figure 3(a)). This narrow peak was also observed as being shifted by Δf_T during the next run at I_4 = I_1 (Figure 3(b)). Note that, at the lowest irradiation power I_1, the sample temperature remains close to the room temperature. This has been proven in separate experiments, in which, after recording the spectrum at I_4, two more spectra were measured using 5% and 1% of the maximum laser intensity. The Raman peak frequency for these two
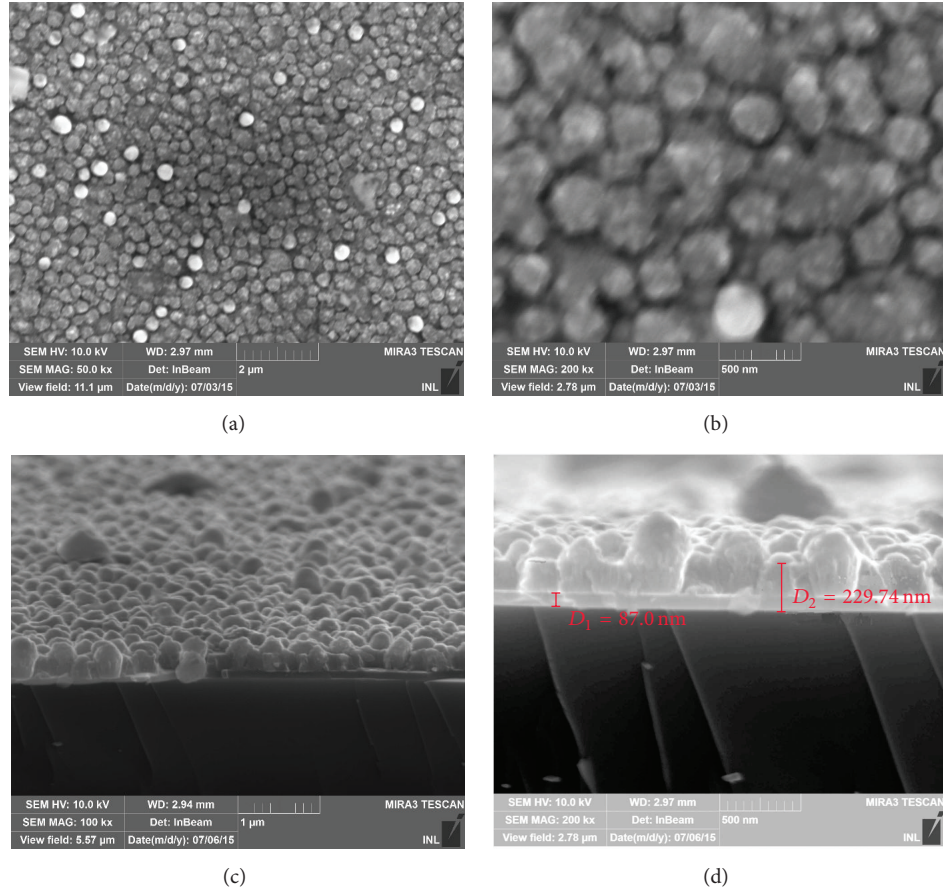
(a)

(b)

(c)

(d)

FIGURE 2: SEM images of the 3-layer structure Si/Sn/Si (region A in Figure 1). The thicknesses of the deposited layers were $X:Y:Z =$ $100:50:100$ nm. Panels (a) and (b) are images of the surface with different magnification. Panels (c) and (d) are tilted images of the chipped surface.

low-intensity runs changed by less than $1\,\mathrm{cm}^{-1}$ in comparison with that for I_4 (the corresponding spectra are not shown in the figures). The narrow peak at 490–$520\,\mathrm{cm}^{-1}$ corresponds to the nanocrystalline silicon phase [26, 27] and the above results evidenced formation of nc-Si as a result of the laser annealing. At the same time, the data collected from region B of the sample during all experimental runs contained only the features attributed to α-Si (not shown in the figure).

The features of the spectrum evolution with laser annealing presented above were similar to those recorded recently during the thermal annealing of Sn:Si layered structures [20], suggesting that the presence of tin in the investigated layered structure facilitates formation and growth of silicon nanocrystals through the mechanism of metal-induced crystallization [21, 22].

Note that crystallization of amorphous Si under the influence of laser radiation has been observed by many researchers [31–34]. It is believed that laser-induced crystallization proceeds through local heating of α-Si by laser beam to a temperature above $1000°$C [31–33], or due to the so-called "cold melting" of Si under short but powerful laser pulses $(10^{11}$–$10^{12}\,\mathrm{W\,cm^{-2}})$ [34–36]; in any case the crystallization is considered to proceed through a thermal mechanism. However, in our case the laser power was not high enough

for a pure thermal crystallization. This is evidenced by the absence of the crystalline Si Raman band for the B region of the samples (outlined in Figure 1) even after multiple Raman runs/scans at a maximum power of the laser radiation.

The crystallites sizes were evaluated from the shift of the crystalline phase Raman peak using a classical phonon confined model [26, 27, 37]. In addition, the content of the nanocrystalline fraction was evaluated from the ratio of the crystalline/amorphous bands areas. The representative results of analysis are summarized in Table 1. The second column of the table shows the thickness of the layers $X:Y:Z$ in nanometers. The third column shows the frequency f of the Raman peak for the crystalline phase at the lowest irradiation power $I_1 = 0.1I_0$ and the increased power $I = kI_0$. The coefficient k values are shown in the fourth column. The fifth and sixth columns summarize the temperature shift Δf_T of the crystalline phase Raman peak and the estimated maximum local temperature T of the material within the laser spot during experimental runs (scans) [30], respectively (see below for more details on estimation of these parameters). The number of 30-second runs (scans) for each sample is shown in the seventh column. The shift Δf_R of the crystalline phase Raman peak position caused by the size-confinement effects at room temperature compared to the peak position

TABLE 1: Results of Raman spectra analysis for different samples.

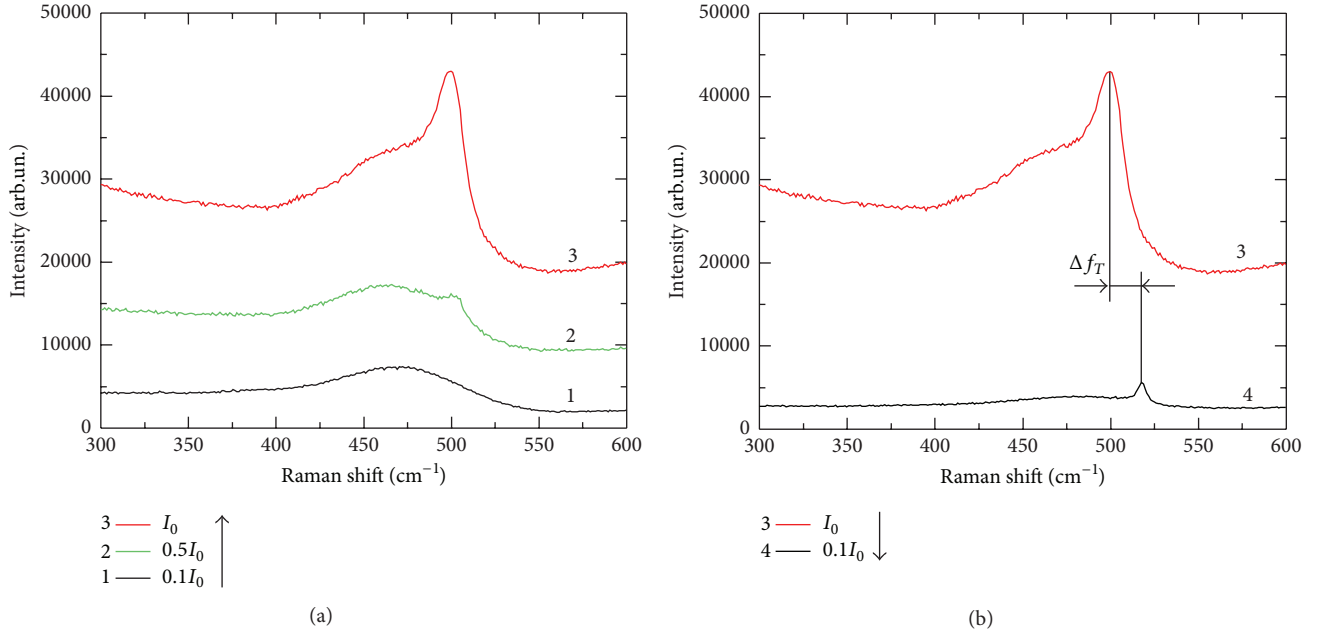| 1	2	3	4	5	6	7	8	9	10
Sample number	$X:Y:Z$ [nm]	f at $0.1I_0/kI_0$ [cm^{-1}]	k	Δf_T [cm^{-1}]	T [°C]	Number of runs/scans	Δf_R [cm^{-1}]	R [nm]	X_C [%]
1	50 : 100 : 200	508/502	0.5	6	250	5	12.0	1.9	92
2	100 : 100 : 100	516/494	1.0	22	960	1	4.0	3.5	90
3	100 : 100 : 200	511/500	0.5	11	480	2	9.0	2.2	92
4	100 : 200 : 100	518/499	1.0	18	830	1	2.5	5.0	86
5	150 : 100 : 50	517/497	1.0	20	870	1	3.0	4.3	81
6	200 : 200 : 200	517/494	1.0	22	960	5	3.0	4.3	80

FIGURE 3: Raman spectra of the sample recorded from the surface in region A. (a) Irradiation intensity run-to-run increased from $0.1I_0$ to $0.5I_0$ and further to I_0. (b) Irradiation intensity run-to-run decreased from I_0 to $0.1I_0$. The layers thicknesses in the sample were $X:Y:Z = 100:50:100$ nm.

for the bulk monocrystalline silicon ($f_R = 520$ cm^{-1}) is given in the eighth column. Note that analysis of the Raman shift Δf made in this work was based solely on size-confinement effects. However, α-Si crystallization induces also a tensile stress due to density difference between the crystalline and amorphous phases of Si [24], which also may affect the Raman shift. This effect requires special studies since the results of our work do not allow quantification of the tensile stress effect on Raman spectra. The dominant size R of nanocrystals and the partial volume X_C of the nanocrystalline phase in the sample as estimated using the methods described previously [25, 26, 37] are presented in columns nine and ten, respectively.

The nanocrystalline phase fraction (partial volume) increased with the laser exposure time. As an example, the dependence of Raman spectra on the exposure time (total time of the runs) is presented in Figure 4. The data in Figure 4 were collected during the first (1), second (2), and fifth (5) run (scan) of the spectrum within the same

location on the surface. The duration of each scan was 30 sec.

The increase of the crystalline phase partial volume with irradiation (exposure) time showed a tendency to saturation. The exposure time at which saturation was observed depended on the initial ratio of the layers thickness (X, Y, and Z). Column 10 of Table 1 presents the final value of the nanocrystalline phase partial volume X_C for each sample.

The crystallization of amorphous silicon under laser irradiation is well studied in the literature [31–36]. Several mechanisms of such crystallization were discussed; among them is the mechanism that relies on an excessive heating of α-Si (thermal mechanism). This mechanism takes advantage of high temperature heating of α-Si close to or above the temperature of crystallization (~1000°C). Such heating can be produced with the continuous wave and/or high power pulsed laser radiation.

Let us evaluate the material's temperature within the laser irradiation spot in our experiments. For this purpose,
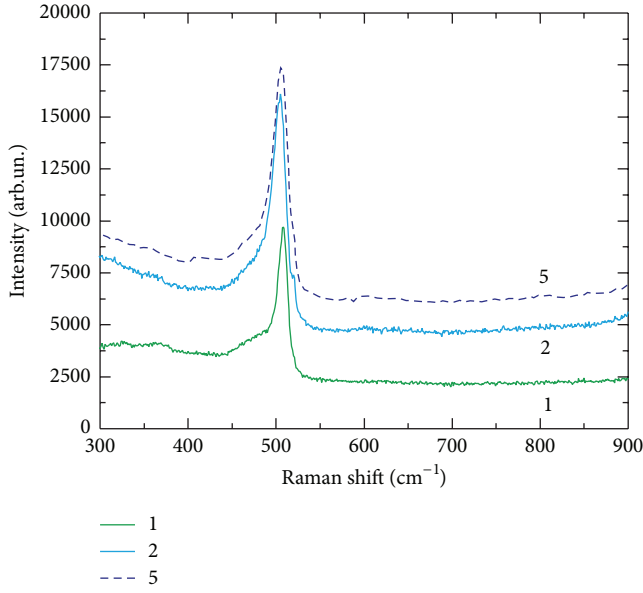
FIGURE 4: Raman spectra of the sample $X : Y : Z = 50 : 100 : 200$ nm at $I = I_0$ recorded during the first (1), second (2), and fifth (5) scan of the same place of the sample.

consider the sample that consists of two layers, a top layer Sn/α-Si composite and a bottom substrate layer. Assume the top composite layer Sn/α-Si is characterized with the average thermal conductivity K_c and optical absorption coefficient $\alpha_c(z)$ whereas the substrate layer is a glass with the thermal conductivity K_s and absorption coefficient α_s. For simplicity, we neglect the light absorption in the substrate ($\alpha_s = 0$ cm^{-1}). The temperature distribution in this case can be evaluated from Fourier's law based thermal conductivity equation

$$
\frac{1}{\rho} \frac{\partial}{\partial \rho} \left(K(z) \rho \frac{\partial \theta}{\partial \rho} \right) + \frac{\partial}{\partial z} \left(K(z) \frac{\partial \theta}{\partial z} \right)
$$
$$
= -I \cdot g(z) \exp \left(\frac{-2\rho^2}{b^2} \right),
\tag{1}
$$

where ρ and z are the lateral and in-depth coordinates, respectively; $K(z)$ is a spatial dependence of the thermal conductivity:

$$
K(z) = \begin{cases} K_c, & z < X + Y + Z, \\ K_s, & z > X + Y + Z. \end{cases}
\tag{2}
$$

$\theta = T - T_0$ is a laser-induced temperature rise; α is an optical absorption coefficient; b is a beam radius and $g(z)$ is a function describing the heat source distribution in the depth of the sample. In our case $g(z)$ can be written as follows:

$$
g(z) = \begin{cases} \alpha \exp(-\alpha z), & z < X + Y + Z, \\ 0, & z > X + Y + Z. \end{cases}
\tag{3}
$$

Equation (3) was applied to estimate the temperature in the irradiated zone. For the optical absorption coefficient α, the

value averaged over the sample thickness was used ($\alpha = (1/l_{\text{abs}}) \int_0^{l_{\text{abs}}} \alpha_c(z) dz$, l_{abs} is the $1/e$ absorption depth for the composite layered structure, whose value was varied for each sample). Thus, for estimation of α, the impact of both α-Si layers and Sn layer was considered and possible increased heat dissipation within the Sn layer was indirectly taken into account, which is important since the absorption coefficient of metallic Sn may be comparable to or even higher than that of α-Si at 633 nm [38, 39].

Equation (1) was written in the cylindrical coordinates, with the ρ-axis parallel and z-axis perpendicular to the sample's surface. The origin coordinate was chosen in the epicenter of the laser irradiation spot at the sample's surface. As the boundary conditions, absence of the heat outflow from the upper surface and the limitation of the solution at the infinity were chosen. In this case

$$
K_c \left. \frac{\partial \theta}{\partial z} \right|_{z=0} = 0,
$$
$$
\theta|_{z,\rho \to \infty} = 0.
\tag{4}
$$

Additionally, the boundary conditions were supplemented with the discontinuity conditions for the heat flux and temperature at the interface between the composite and glass substrate. In this case, the solution of (1) can be presented as follows:

$$
\theta = \int_0^\infty \theta^H(\lambda z) \cdot J_0(\lambda \rho) \rho \, d\rho,
\tag{5}
$$

where θ^H is a Hankel transform of θ; λ is a positive real number; J_0 is a zero-order Bessel function of the first kind. The value of θ^H was determined from the Hankel transformation of (1)

$$
\frac{d}{dz} \left(K(z) \frac{d\theta^H}{dz} \right) - \lambda^2 K(z) \theta^H
$$
$$
= -I \cdot g(z) \frac{4}{b^2} \exp \left(-2 \frac{\lambda^2}{b^2} \right),
\tag{6}
$$

and using the appropriate boundary conditions.

Typical results of the surface temperature simulation are presented in Figure 5(a). In accordance with simulations, the temperature even at the epicenter (~850°C) was not high enough to induce fast processes of the thermal crystallization. Taking into account the absence of the crystalline peak in B region of the sample, we concluded that silicon nanocrystallites in our experiments were formed as a result of tin induced crystallization of amorphous silicon. As was mentioned above, the temperature required to trigger such crystallization is close to Sn melting temperature (T_m ~ 230°C). As is obvious from Figure 5(a), the regions with the temperature higher than T_m correlate well with the regions of the laser-induced surface modification imaged using the optical microscope (see Figure 5(b)).

As is known, the position of the Raman peak depends on the sample temperature. In the crystalline silicon, the Raman peak shifts linearly towards lower frequencies with
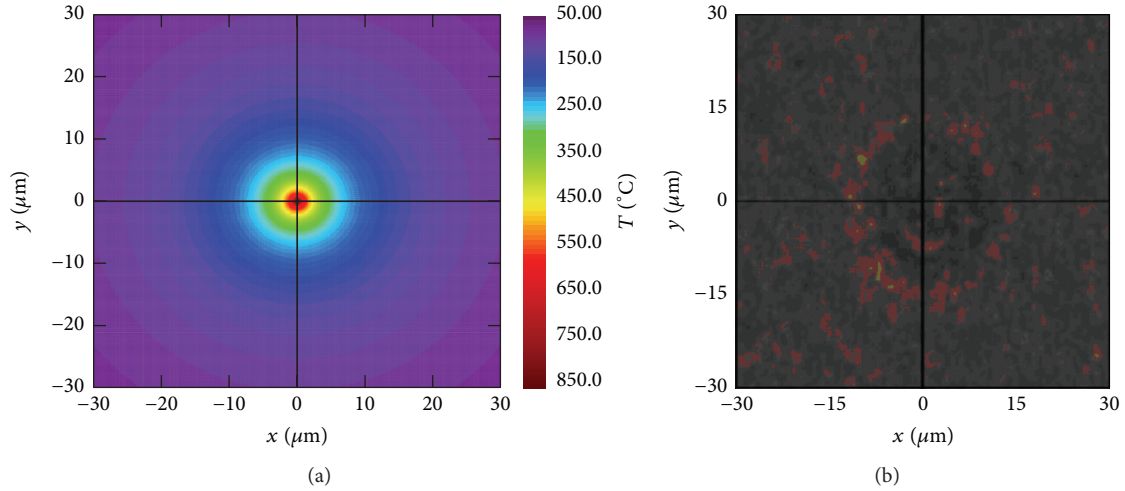
FIGURE 5: (a) Simulation results of the temperature filed distribution on the surface of the sample. (b) Optical microscope image of the sample surface after 5 laser scans.
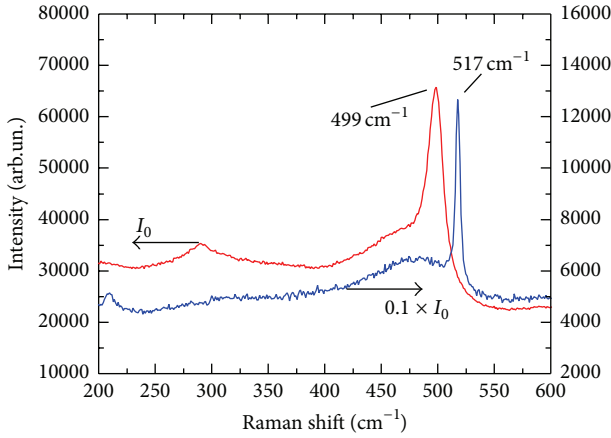

FIGURE 6: Raman spectra of a sample having the ratio $X:Y:Z$ = 100 : 200 : 100 nm. The left axis corresponds to the spectrum recorded using a maximum laser power ($I = I_0$); the right axis corresponds to the spectrum recorded using a minimum power ($I = 0.1 I_0$).

the temperature increase. Figure 6 shows an example of the temperature shift of nc-Si Raman peak observed in our experiments. Note different y-axis scales for the two spectra in Figure 6 as opposed to a single scale in Figure 3(b) where the temperature shift was marked as Δf_T.

The dependence of the Raman peak shift on temperature summarized in column 5 of Table 1 allowed evaluating the local temperature T within the region heated by the laser beam (column 6 of Table 1). This local temperature varied within the range from 350°C to 960°C for different samples and depended on the ratio $X:Y:Z$. A relatively large variation in the local temperature for different samples can be explained by varying conditions of optical absorption and heat outflow from the laser-illuminated zone.

4. Conclusions

Results of this work demonstrated laser-induced crystallization of Sn/(α-Si) layered structures at relatively low temperatures. We suggest that the MIC mechanism described in details recently [21, 22] is also valid for the laser-induced crystallization observed in this work. The results showed that Si nanocrystals formation rate, their size, and concentration are controlled by the local temperature within the laser spot and duration of the heating process and, therefore, depend on the irradiation power and exposure time to laser radiation. We demonstrated that the in situ analysis of Raman spectra during laser annealing allows for the in-line control of the crystallites size and partial volume of nc-Si. The number and thickness of Si and Sn layers in the starting material (sample) may be considered as the technological factors that determine the overall thickness of the amorphous-crystalline composite film, distribution of nanocrystals in it, and the amount and status of the residual tin, which is important for the development of new technologies for the solar cell materials.

Since recently, MIC in general and laser-induced MIC in particular attracted steadily increased interest for photovoltaic applications. Our present studies demonstrated the feasibility of nc-Si thin films fabrication with the in situ controlled band gap, which may be an alternative, ecologically friendly solution for the solar cells technology. Utilization of tin for the MIC process is advantageous because in contrast to many other metals, it does not create energy levels within the forbidden zone of nanocrystals, facilitating thereby a decrease of losses in photoelectric transformation of solar radiation. Thermal evaporation in vacuum applied for the layers deposition in this work is also advantageous in comparison with traditional CVD methods since it allows not only excluding hydrogen from the process, but also significantly simplifying and making the manufacturing of nc-Si thin films more cost-effective. One more important feature of thin nc-Si films is their nanostructured surface that minimizes the energy loss due to light reflection from

the surface. All abovementioned properties may facilitate application of the technology described in this work for efficient and cost-effective photovoltaic applications.

Competing Interests

The authors declare that they have no competing interests.

Acknowledgments

References

[1] M. C. Beard, J. M. Luther, and A. J. Nozik, "The promise and challenge of nanostructured solar cells," *Nature Nanotechnology*, vol. 9, no. 12, pp. 951–954, 2014.

[2] Z. I. Alferov, V. M. Andreev, and V. D. Rumyantsev, "Solar photovoltaics: trends and prospects," *Semiconductors*, vol. 38, no. 8, pp. 899–908, 2004.

[3] B. Yan, G. Yue, X. Xu, J. Yang, and S. Guha, "High efficiency amorphous and nanocrystalline silicon solar cells," *Physica Status Solidi*, vol. 207, no. 3, pp. 671–677, 2010.

[4] N. S. Lewis, "Toward cost-effective solar energy use," *Science*, vol. 315, no. 5813, pp. 798–801, 2007.

[5] R. Søndergaard, M. Hösel, D. Angmo, T. T. Larsen-Olsen, and F. C. Krebs, "Roll-to-roll fabrication of polymer solar cells," *Materials Today*, vol. 15, no. 1-2, pp. 36–49, 2012.

[6] M. Birkholz, B. Selle, E. Conrad, K. Lips, and W. Fuhs, "Evolution of structure in thin microcrystalline silicon films grown by electron-cyclotron resonance chemical vapor deposition," *Journal of Applied Physics*, vol. 88, no. 7, pp. 4376–4379, 2000.

[7] B. Rech, T. Roschek, J. Müller, S. Wieder, and H. Wagner, "Amorphous and microcrystalline silicon solar cells prepared at high deposition rates using RF (13.56 MHz) plasma excitation frequencies," *Solar Energy Materials and Solar Cells*, vol. 66, no. 1–4, pp. 267–273, 2001.

[8] M. K. van Veen, C. H. M. van der Werf, and R. E. I. Schropp, "Tandem solar cells deposited using hot-wire chemical vapor deposition," *Journal of Non-Crystalline Solids*, vol. 338–340, no. 1, pp. 655–658, 2004.

[9] Y. Mai, S. Klein, R. Carius et al., "Improvement of open circuit voltage in microcrystalline silicon solar cells using hot wire buffer layers," *Journal of Non-Crystalline Solids*, vol. 352, no. 9–20, pp. 1859–1862, 2006.

[10] H. Li, R. H. Franken, R. L. Stolk, C. H. M. van der Werf, J. K. Rath, and R. E. I. Schropp, "Controlling the quality of nanocrystalline silicon made by hot-wire chemical vapor deposition by using a reverse H_2 profiling technique," *Journal of Non-Crystalline Solids*, vol. 354, no. 19–25, pp. 2087–2091, 2008.

[11] R. Amrani, F. Pichot, L. Chahed, and Y. Cuminal, "Amorphous-nanocrystalline transition in silicon thin films obtained by argon diluted silane PECVD," *Crystal Structure Theory and Applications*, vol. 1, pp. 57–61, 2012.

[12] G. Fugallo and A. Mattoni, "Thermally induced recrystallization of textured hydrogenated nanocrystalline silicon," *Physical Review B*, vol. 89, no. 4, Article ID 045301, 10 pages, 2014.

[13] O. Nast and A. J. Hartmann, "Influence of interface and Al structure on layer exchange during aluminum-induced crystallization of amorphous silicon," *Journal of Applied Physics*, vol. 88, no. 2, pp. 716–724, 2000.

[14] M. Jeon, C. Jeong, and K. Kamisako, "Tin induced crystallisation of hydrogenated amorphous silicon thin films," *Materials Science and Technology*, vol. 26, no. 7, pp. 875–878, 2010.

[15] M. A. Mohiddon and M. G. Krishna, "Growth and optical properties of Sn–Si nanocomposite thin films," *Journal of Materials Science*, vol. 47, no. 19, pp. 6972–6978, 2012.

[16] D. Van Gestel, I. Gordon, and J. Poortmans, "Aluminum-induced crystallization for thin-film polycrystalline silicon solar cells: achievements and perspective," *Solar Energy Materials and Solar Cells*, vol. 119, pp. 261–270, 2013.

[17] A. Mohiddon and G. Krishna, "Metal induced crystallization," in *Crystallization—Science and Technology*, A. Marcello, Ed., pp. 461–480, InTech, 2012.

[18] V. V. Voitovych, V. B. Neimash, N. N. Krasko et al., "The effect of Sn impurity on the optical and structural properties of thin silicon films," *Semiconductors*, vol. 45, no. 10, pp. 1281–1285, 2011.

[19] V. B. Neimash, V. M. Poroshin, A. M. Kabaldin et al., "Microstructure of thin Si–Sn composite films," *Ukrainian Journal of Physics*, vol. 58, no. 9, pp. 865–871, 2013.

[20] V. Neimash, V. Poroshin, P. Shepeliavyi et al., "Tin induced a-Si crystallization in thin films of Si-Sn alloys," *Journal of Applied Physics*, vol. 114, no. 21, Article ID 213104, 2013.

[21] V. B. Neimash, A. O. Goushcha, P. E. Shepeliavyi et al., "Mechanism of tin-induced crystallization in amorphous silicon," *Ukrainian Journal of Physics*, vol. 59, no. 12, pp. 1168–1176, 2014.

[22] V. B. Neimash, A. O. Goushcha, P. Y. Shepeliavyi et al., "Self-sustained cyclic tin induced crystallization of amorphous silicon," *Journal of Materials Research*, vol. 30, no. 20, pp. 3116–3124, 2015.

[23] G. L. Olson and J. A. Roth, "Kinetics of solid phase crystallization in amorphous silicon," *Materials Science Reports*, vol. 3, no. 1, pp. 1–77, 1988.

[24] M. D. Efremov, V. V. Bolotov, V. A. Volodin, L. I. Fedina, and E. A. Lipatnikov, "Excimer laser and rapid thermal annealing stimulation of solid-phase nucleation and crystallization in amorphous silicon films on glass substrates," *Journal of Physics: Condensed Matter*, vol. 8, no. 3, pp. 273–286, 1996.

[25] S. Sriraman, S. Agarwal, E. S. Aydil, and D. Maroudas, "Mechanism of hydrogen-induced crystallization of amorphous silicon," *Nature*, vol. 418, no. 6893, pp. 62–65, 2002.

[26] H. Richter, Z. P. Wang, and L. Ley, "The one phonon Raman spectrum in microcrystalline silicon," *Solid State Communications*, vol. 39, no. 5, pp. 625–629, 1981.

[27] I. H. Campbell and P. M. Fauchet, "The effects of microcrystal size and shape on the one phonon Raman spectra of crystalline semiconductors," *Solid State Communications*, vol. 58, no. 10, pp. 739–741, 1986.

[28] M. Balkanski, R. F. Wallis, and E. Haro, "Anharmonic effects in light scattering due to optical phonons in silicon," *Physical Review B*, vol. 28, no. 4, pp. 1928–1934, 1983.

[29] B. Stoib, S. Filser, N. Petermann, H. Wiggers, M. Stutzmann, and M. S. Brandt, "Thermal conductivity of mesoporous films measured by Raman spectroscopy," *Applied Physics Letters*, vol. 104, no. 16, Article ID 161907, 2014.

[30] S. Périchon, V. Lysenko, B. Remaki, D. Barbier, and B. Champagnon, "Measurement of porous silicon thermal conductivity by micro-Raman scattering," *Journal of Applied Physics*, vol. 86, no. 8, pp. 4700–4702, 1999.

[31] S. Chen and I. C. Hsieh, "Polysilicon TFT technology will solve problems of mobility, pixel size, cost, and yield," *Solid State Technology*, vol. 39, pp. 113–120, 1996.

[32] A. A. D. T. Adikaari and S. R. P. Silva, "Thickness dependence of properties of excimer laser crystallized nano-polycrystalline silicon," *Journal of Applied Physics*, vol. 97, no. 11, Article ID 114305, 2005.

[33] T. Y. Choi, D. J. Hwang, and C. P. Grigoropoulos, "Ultrafast laser-induced crystallization of amorphous silicon films," *Optical Engineering*, vol. 42, no. 11, pp. 3383–3388, 2003.

[34] J.-M. Shieh, Z.-H. Chen, B.-T. Dai, Y.-C. Wang, A. Zaitsev, and C.-L. Pan, "Near-infrared femtosecond laser-induced crystallization of amorphous silicon," *Applied Physics Letters*, vol. 85, no. 7, pp. 1232–1234, 2004.

[35] V. A. Volodin and A. S. Kachko, "Crystallization of hydrogenated amorphous silicon films by exposure to femtosecond pulsed laser radiation," *Semiconductors*, vol. 45, no. 2, pp. 265–270, 2011.

[36] A. V. Emelyanov, A. G. Kazanskii, P. K. Kashkarov et al., "Effect of the femtosecond laser treatment of hydrogenated amorphous silicon films on their structural, optical, and photoelectric properties," *Semiconductors*, vol. 46, no. 6, pp. 749–754, 2012.

[37] E. Bustarret, M. A. Hachicha, and M. Brunel, "Experimental determination of the nanocrystalline volume fraction in silicon thin films from Raman spectroscopy," *Applied Physics Letters*, vol. 52, no. 20, pp. 1675–1677, 1988.

[38] K. Takeuchi and S. Adachi, "Optical properties of β-Sn films," *Journal of Applied Physics*, vol. 105, no. 7, Article ID 073520, 2009.

[39] Y. Hishikawa, N. Nakamura, S. Tsuda, S. Nakano, Y. Kishi, and Y. Kuwano, "Interference-free determination of the optical absorption coefficient and the optical gap of amorphous silicon thin films," *Japanese Journal of Applied Physics, Part 1*, vol. 30, no. 5, pp. 1008–1014, 1991.